The final publication is available at

https://doi.org/10.1016/j.compstruct.2022.115265

Additional Information

Modeling the delamination failure compressive loads in CFRP laminates based on digital image correlation analysis.

J. V. Calvo[1]*, N. Feito[2], M. H. Miguelez[1], E. Giner[2].

[1] Department of Mechanical Engineering, University Carlos III of Madrid, Avda. Universidad 30, 28911 Leganés, Madrid, Spain

[2] Institute of Mechanical and Biomechanical Engineering - I2MB, Department of Mechanical and Materials Engineering, Universitat Politècnica de València, Camino de Vera, 46022 Valencia, Spain

*corresponding author: jocalvoo@ing.uc3m.es

Abstract

L aminate composite materials such as CFRPs are highly susceptible to delamination, being one of the common failure modes in composite laminates. The combination of severe delamination with uniaxial compressive loads leads to the loss of stability and structure failure. In this study, the authors present an experimental and numerical analysis of this effect in laminates. A series of tests were carried out with four different specimens including delamination-free plates and plates with incipient delamination with different damage size and location. 3D Digital Imagen Correlation technique was applied to predict the buckling initiation and propagation and to validate the numerical models implemented, showing good agreement between the numerical and experimental results. Model material failure includes Hashin criterion and cohesive zone model (CZM) to predict delamination. Finally, numerical models have been used to predict the crack initiation and progression in the rest of samples.

Keywords: CFRP composites, Compression test, FEM analysis, numerical model, digital image correlation.

1. Introduction

CFRP materials exhibiting high strength/stiffness-to-weight ratios have been increasingly used in the manufacturing of responsibility structures in aerospace engineering and other fields during last decades. However, due to the anisotropic behavior generated by the fibers orientation, the study of failure modes are complicated, being the delamination damage the most significant failure mechanism [1]. This defect can be related to manufacturing fault [2–4], free edge effect [5,6], or impact by a foreign object [7–10] affecting the mechanical response of the composite component. The possibility of the uncontrolled growth of existing delamination is an important problem frequently addressed in the literature [11–16].

Failure of composite laminates can be described through the simple theory of the first ply failure theory (FPF) [17] which considers the laminate failure when the first layer of the laminate is damaged. Damage state in these structures can be observed experimentally using techniques as ultrasonic C-scan [10,18,19], X-ray radiography [20–22], acoustic emission [23,24], ultrasonic testing [25–27] or Digital Image Correlation (DIC) [3,8,24,27]. Once the location and the extent

of the defects are identified, the main concern is to determine their influence on the mechanical properties of the material.

The damage initiation assessment in numerical calculations can be performed using the Hashin failure criterion [28]. This criterion identifies four different failure modes for the composite material: tensile fiber failure, compressive fiber failure, tensile matrix failure, and compressive matrix failure. The damage initiation is related to the reach of initial critical parameters of the composite material for each one of the failure modes. Combining the Hashin criterion with stiffness degradation, the damage progression can be conducted. The Hashin criterion has been succesfully implemented in the literature for CFRP studies [3,29–31].

Study of delamination is especially relevant under in-plane compressive loading, where the propagation of an interlaminar flaw is promoted. New methods of analysis and evaluation of the complex structures and multi-load cases studies have been reported in the literature [29,32–34]. Analysis of buckling of laminated structures have defined three stages of damage in the full range of loads. In the first stage, the damage of the composite material is initiated. During the second stage, damage evolution grows generating a mixed or global buckling mode, which depends on the size and location of the delamination in the thickness direction of the laminate. The occurrence of instability phenomenon depends on several parameters as the delamination geometry, ply material properties, or the stacking sequence of the laminate [35–38]. In the final stage, the structure collapses. The three buckling mode shapes can be observed in Fig. 1.
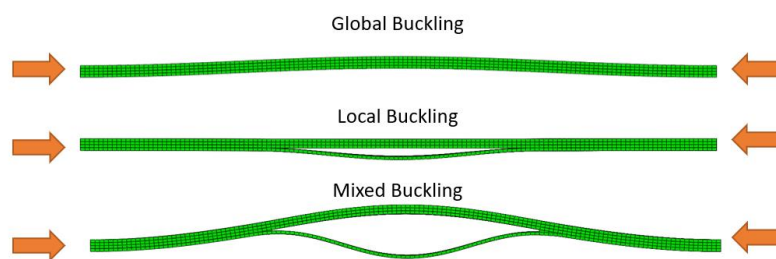
Figure 1: Three buckling mode shapes.

Under uniaxial compressive loading, delamination generally causes an increase in the Strain Energy Release Rate (SERR). When the energy for the propagation of the delamination reaches the critical level, delamination grows leading to further stiffness loss, and consequently larger deflections. The fracture Mode II (shearing) appears when SERR rises due to a global buckling. The combination of Mode I (opening) and Mode II occurs in local or mixed buckling mode shapes [16]. The Strain Energy Release Rate has been calculated by several authors (see for instance Chai et al. [39], Bruo et al. [40], K¨ollner et al. [41]). All authors calculated the SERR as the first variation of the total strain energy of the structure with respect to the length of the delaminated region.

However, most formulations for predicting the post-buckling behavior of delaminated composite plates are based on the Crack Extension Techniques (CET) for calculating SERR. The CET determines the total SERR as the difference between the strain energies of the plate before and after an infinitesimal advancement of the crack front per unit surface area of the newly cracked region [16] and it has been implemented in one dimensional and two-dimensional analyses for Finite Element Method (FEM) allows developing more complex

techniques as the Virtual Crack Closure Technique (VCCT) [47,48] and Cohesive Zone Models (CZMs) [49,50] for modeling the progressive growth of delamination. VCCT involves the

assumption that energy released during the crack growth is equal to the energy required for closing it. This technique can determine the energy release rates corresponding to the three simple fracture modes [48,51–54]. CZMs assign a decohesive constitutive law to an imaginary interface located in the delamination plane. CZMs predict both the damage initiation and delamination damage evolution and it was successfully implemented in linear elastic and elasto-plastic crack propagation problems [55–61].

This paper presents the results of experimental tests of CFRP composite laminates with initial delamination. Specimens were manufactured through the autoclave technique and subsequently subjected to axial compression in the full range of loading conditions up to failure. 3D Digital Imagen Correlation technique was used to detect the buckling initiation and propagation. The tested specimen was modeled using the finite element method (FEM) with the CZM approach and the Hashin failure criteria. Numerical predictions were compared with the DIC results for validation. Finally, numerical investigations were analyzed to discuss the effects of initial delamination size and location on the buckling mode intralaminar damage. rectangular delamination [42–44] and elliptical delamination [45,46].

2. Materials and experimental set-up

All specimens are cut from a flat laminate with four unidirectional carbon/epoxy layers made of SparPreg™ prepregs supplied by Gurit company and manufactured through autoclave. The dimensions of the plates are 140 × 20 mm with a total thickness of 1.3 mm. The mechanical properties of one ply are listed in Table 1 where the subscript 1 represents the fiber direction and 2 the direction transverse to the fiber. At both ends of the composite laminate specimen tabs of 35 mm were added following the D3410/D3410M standard recommendation [62], restricting the effective length (L) of the experimental specimen where the delamination can propagate to 70 mm.

Fiber volume	ρ	E_{1t}	E_{2t}	E_{1c}	E_{2c}	G_{12}
66 %	1.55 g/cm3	140 GPa	7.9 GPa	123 GPa	7.2 GPa	4.9 GPa
υ_{12}	X_t	Y_t	X_c	Y_c	S_l	S_t
0.79	2234 MPa	45 MPa	1183 MPa	146 MPa	51 MPa	81 MPa

Table 1 Mechanical properties of the one CFRP ply provided by Gurit.

(a) No delamination   **(b) Middel plane delamination**

(c) Upper-ply delamination   **(d) Upper-ply delamination**
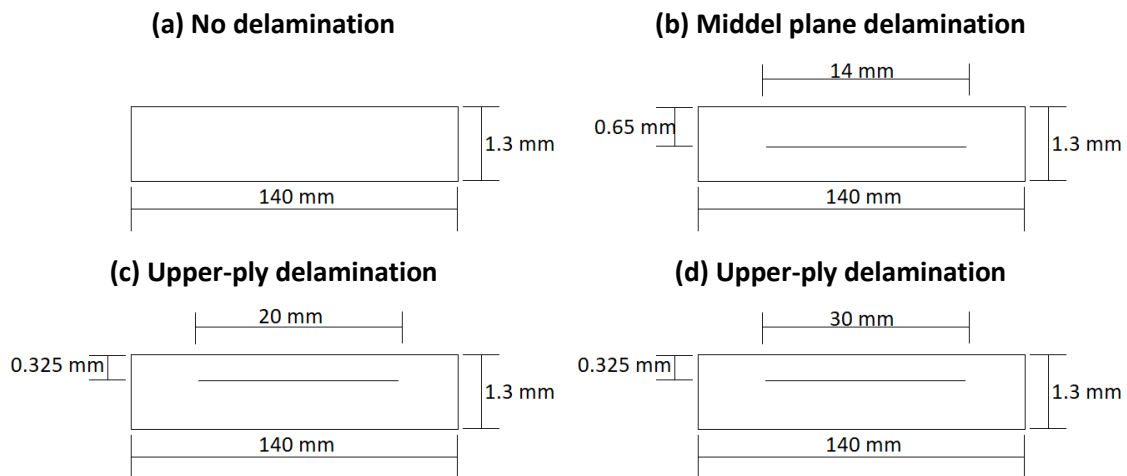
Figure 2: Scheme of the different specimens used in this study.

A scheme of the specimens with different configurations of delamination shapes and locations considered in this work is shown in Fig. 2. The first configuration does not include any damage in the laminate. The second, third and fourth configurations (Fig. 2 (b), (c) and (d) respectively) correspond to specimens with induced delamination. Specimens (c) and (d) were manufactured with the same delamination location but with different size. These defects have been generated placing during laminate manufacturing a 0.025 mm thick Teflon sheet with the length indicated for each case.

Buckling tests were carried out in an electro-mechanic testing machine, MTS C42.503, equiped with a load cell of 5 kN. Clamps were used to fix the initial position avoiding sliding and rotation during the application of compressive load. The Digital Image Correlation technique (DIC) was used to obtain the displacement field on the up layer of the laminate during quasi-static tests. This non-destructive methodology is based on optical displacement measurement using image pattern tracking for accurate 3D surface deformation measurements during testing. The DIC technique divides the region of interest (ROI) in squared faces to track their displacement based on an image pattern matching criterion and compares each deformed image with either the reference or the previous one. A ROI that covered the whole area on the top surface of the specimen was defined. A scheme of the set-up is shown in Fig. 3.
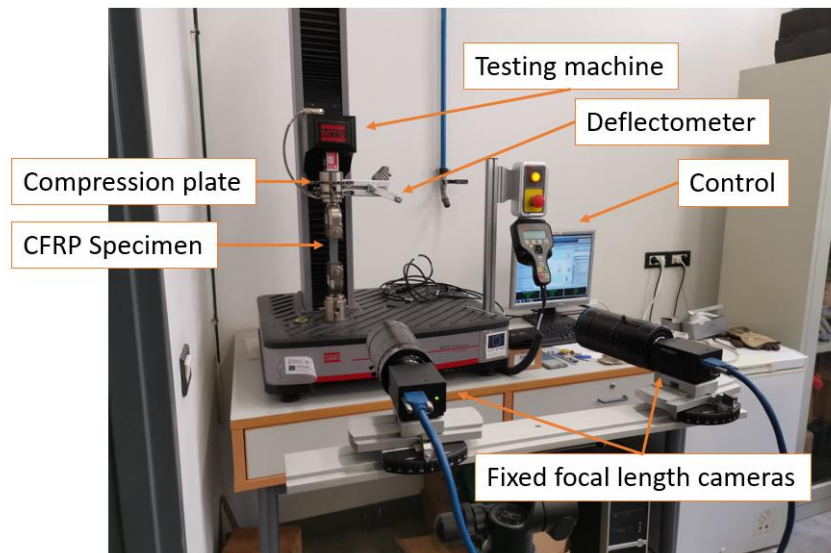
Figure 3: Experimental testing and imaging set-up.

The images were acquired with a high resolution fixed focal lens (HF7518V-2, Myutron, Tokyo, Japan) and extension rings of 10 mm (focal length of 65 mm). The upper layer surface of the specimen was speckled using randomly distributed black and white spray paints to increase contrast, as shown in Fig. 4. Moreover, the quality of the pattern was inspected using VIC-3D Digital Image Correlation software (v.6.0.2 Correlated Solutions Inc., Irmo, SC, USA) to verify optimum speckle pattern on the surface of the specimens.

The cameras were calibrated with images of a standard speckle provided by Correlated Solutions for reference. All tests were performed under displacement control mode and quasistatic conditions, with displacement rate of 1.5 mm/min following the D3410/D3410M standard [62]. The force–displacement data were registered. No pre-load was applied, and all tests were loaded up to final failure of the specimens.

Specimen without speckle

140 mm

Specimen with speckle and tabs

140 mm

70 mm 35 mm
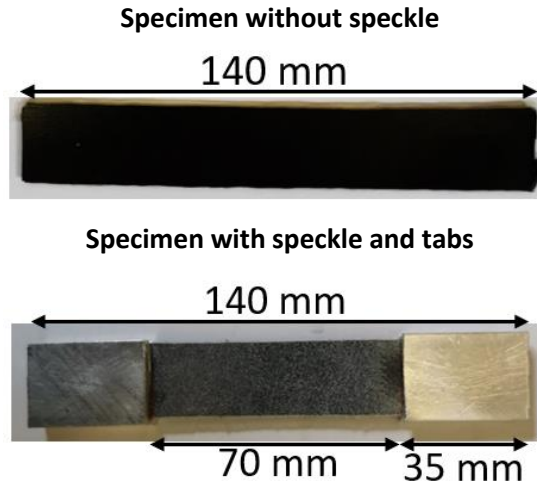
Figure 4: Geometry and preparation of the CFRP specimens.

3. Experimental results and discussion

Two buckling modes were clearly observed during the experiments. Fig. 5 shows both modes: global bucking for the geometries A and B and mixed buckling mode for the geometries C and D. Experimental data are shown in Fig. 6, where the plots force–displacement are represented.

(a)   (b)
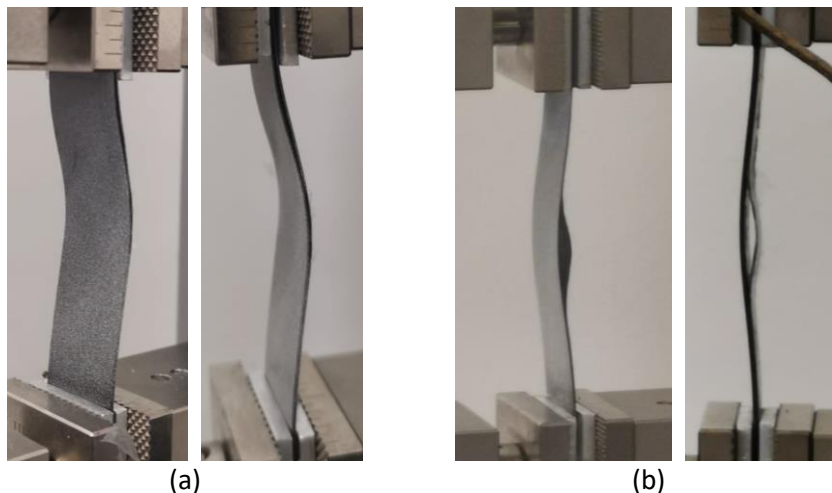
Figure 5: Examples of buckling global mode for geometry B (a) and buckling mixed mode for geometry D (b).

Buckling mode depends on the delamination configuration. Samples A (specimen without delamination) and B (specimen with delamination in the middle plane) present similar behaviour (Fig. 6 (a) and (b) respectively), with buckling occurring in global mode, and the response of both types of specimens are the same at the beginning of the test. In the case of geometry B the global buckling developed with both sublaminates deflecting in the same direction, Fig. 5 (a), as reported in the literature [57,63]. However, it is observed that, following the First Plane Failure Theory, specimens with delamination fail more abruptly than delamination-free specimens.

On the other hand, samples C and D present similar behaviour (Fig. 6 (c) and (d)), but different to configurations A and B. These specimens have delamination in the upper ply, near the free surface, but with different size. During the initial phase of the experiment, local buckling mode was observed in the thinner sub-laminate, as reported in other studies [37,57]. This occurs because the appearance of this local buckling delays and counteracts global buckling, resulting

in reduced specimen bending. This phenomenon is reflected at the initial slope of the plots, more steep in C and D than A and B samples. It can be concluded that plates with upper delamination present a stiffer response than that observed in middle plane delamination specimens, reaching the maximum peak load at lower displacement.
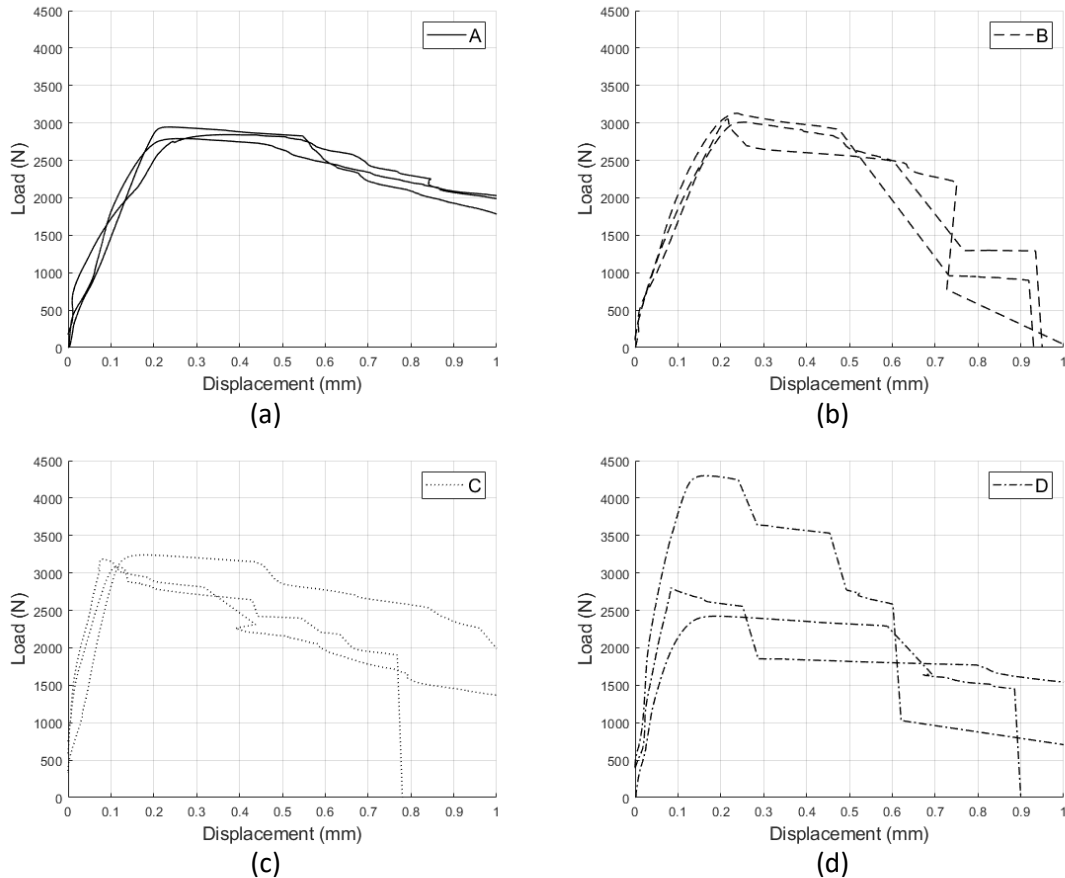

Figure 6: Compressive Force-Displacement curves for the different tested geometries.

As the displacement increases, the resistance in case A is reduced up to the final fiber–matrix breakage as can be seen in Fig. 7 (a). Delamination initiation and propagation was negligible. For geometry B, the deflection occurred in the same direction with delamination mode II being dominant. The peak load is the same observed in case A, and it wasreached at the same displacement. In this case, the delamination propagation generates sudden load drops. Finally, in the geometries with upper-delamination the load peak was reached at lower displacement than the other two cases, due to the local buckling occurred early at smaller applied displacement, generating an opening mode I. The evolution of the buckling mode to mixed buckling changed the delamination mode to shear dominated mode II. The three geometries led to fiber–matrix failure after delamination propagation, see Fig. 7 (b). This behaviour was observed in similar studies [36,57].

During testing, the displacement field of the specimen on the speckled surface was registered. The two cameras used for the DIC and the stereo system allowed to obtain the displacement field in 3 directions, where directions 1 and 2 are in the fiber orientation plane and direction 3 is perpendicular to the plane. An example of the damage evolution in direction 3 of one specimen with geometry C as observed through the 3D DIC methodology is presented in Fig. 8.
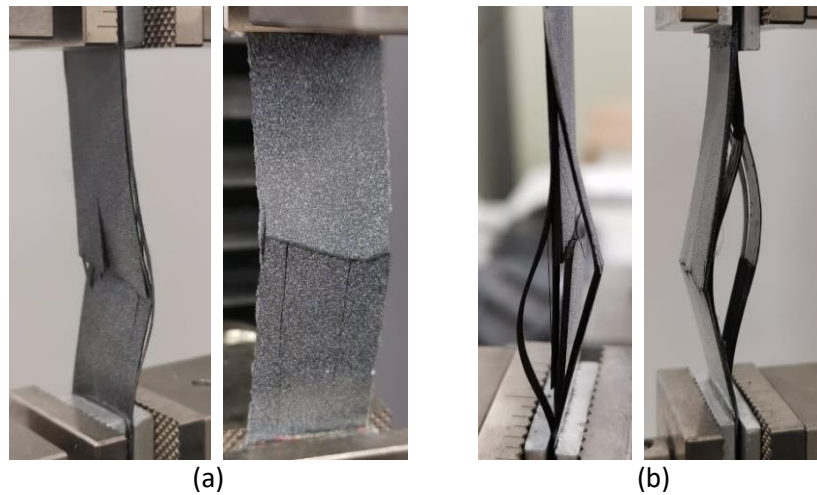
Figure 7: (a) Matrix-Fiber failure for specimen A and (b) combined failure for specimen B (left) and specimen D (right).
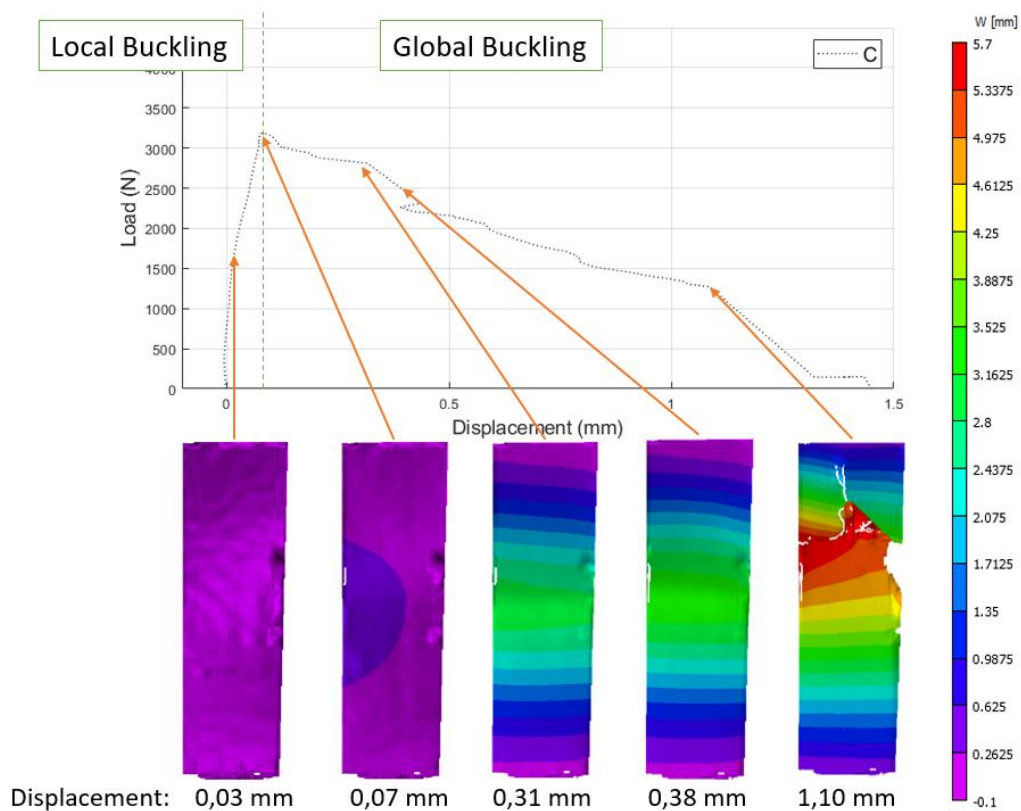

Figure 8: Example of damage evolution in direction 3 visualized with stereo images obtained from DIC 3D.

It is important to highlight the fact that this methodology is capable of detecting the local buckling, as observed in the first two images, where displacement is negative (-0.1 mm). The change in direction due to the global buckling is easy to identify due to the sign change in the displacement value. The area where the breakage occurred could be enclosed. The central deflection of the ply until the collapse could also be determined, equal to 5.7 mm in this example.

4. Numerical model implementation

Finite elements models of each configuration were developed using Abaqus/Standard, aimed at simulating the quasi-static compression tests described previously. Each model reproduces the stacking sequence previously described including the initial delamination damage with the position and length corresponding to each geometry. The laminate is modelled using 3D solid elements C3D8R (8 node-linear brick, reduced integration and hourglass control) with a size of 0.5 mm. One element per ply is defined through the thickness. The adopted boundary conditions are illustrated in Fig. 9.
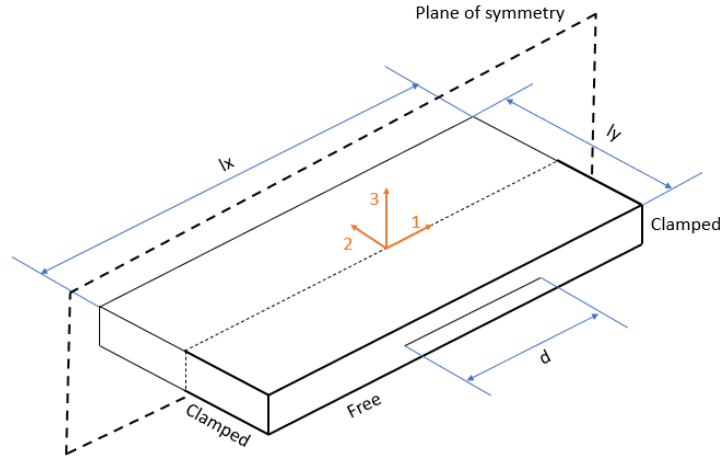
Figure 9: Schematic view of the numerical model implemented for a plate with delamination in the middle plane.

Traction matrix cracking	$$\left(\frac{\sigma_{22} + \sigma_{33}}{Y_t}\right)^2 + \frac{\tau_{23}^2 - \sigma_{22}\sigma_{33}}{S_t^2} + \frac{\tau_{12}^2 + \tau_{13}^2}{S_l^2} = 1$$
Compression matrix cracking	$$\left[\left(\frac{Y_c}{2 S_t}\right)^2 - 1\right]\frac{\sigma_{22} + \sigma_{33}}{Y_c} + \left(\frac{\sigma_{22} + \sigma_{33}}{2 S_t}\right)^2 + \frac{\tau_{23}^2 - \sigma_{22}\sigma_{33}}{S_t^2} + \frac{\tau_{12}^2 + \tau_{13}^2}{S_l^2} = 1$$
Tensión fiber breakage	$$\left(\frac{\sigma_{11}}{X_t}\right)^2 + \frac{\tau_{12}^2 + \tau_{13}^2}{S_l^2} = 1$$
Fiber micro-buckling in compression	$$\frac{-\sigma_{11}}{X_c} = 1$$

Table 2. Hashin failure criterion.

The plies have been modeled assuming an elastic behavior until using the properties detailed in Table 1. The material model was defined through a USDFLD subroutine. The expressions used to define failure in the composite are presented in Table 2 corresponding to the Hashin model [28] and commonly applied in composite materials [3,10,34]. This model considers four different failure modes: fibre failure at tension and compression in direction 1 and matrix failure at tension and compression in direction 2. In the equations σ_{ij} and τ_{ij} are the components of the stress tensor, X_t and X_c are the strengths of the laminate in tension and compression for the fibre direction, Y_t and Y_c are the strengths in tension and compression for the trasverse direction and S_l and S_t are the shear strengths in the different planes (longitudinal and transverse). When the value of this expressions reaches 1, the material is completely damaged and strength is lost, thus some of the stress components are set to zero. The strain tensor is calculated after each time

increment, and when one of the components reaches the critical value, the material properties of that element are degraded.

Cohesive elements COH3D8 were used to simulate delamination progression. A thin layer of 0.001 mm thickness of cohesive elements was inserted along the horizontal planes between every two plies. For each geometry tested, the cohesive zone was modified, removing the elements where the Teflon is located to simulate the initial delamination.

The parameters required for cohesive elements are obtained from previous studies carried out by the research team, providing delamination energy level. Related literature has also been used to correctly estimate the value of the rest of the parameters [58]. These parameters are summarized in Table 3, where G_{IC} is the delamination release energy in mode I obtained from standard DCB tests. The rest of the parameters have been estimated from the literature, where G_{IIC} is the delamination release energy in mode II [54,60,61], K is the stiffness of the cohesive elements [58], σ_n is the maximum normal stress [58], σ_s and σ_t are the maximum stresses in the first and second directions [58] and η is the coefficient of viscous regulation. The criterion selected to calculate the damage initiation is the quadratic nominal stress (QUADS).

G_{IC}	G_{IIC}	K	σ_n	σ_s	σ_t	η
0.361 N/mm	1.083 N/mm	10^5 N/mm^3	20 MPa	40 MPa	40 MPa	10^{-5}

Table 3. Cohesive elements parameters.

5. Numerical model results and discussion

The numerical results obtained from FEM models simulating buckling tests with and without delamination were compared with the experimental predictions of DIC technique. Specifically, both displacement fields in direction 1 and 3 have been compared for the four geometries. Results for configurations A and C are presented in Figs. 10 and 11. It can be observed that the distribution of the field is very similar for all cases and in both directions, which validates the numerical models developed and points out the effectiveness of DIC technique for surface displacement analysis.

| U1 = 0.3 mm	Geometry A	Geometry B	Geometry C	Geometry D
Experimental (DIC)	2.34 mm	2.48 mm	2.65 mm	2.27 mm
Numerical Model prediction	2.79 mm	2.80 mm	2.63 mm	2.33 mm
Error	19.3%	13.1%	0.8%	2.8%
U1 = 0.5 mm	Geometry A	Geometry B	Geometry C	Geometry D
Experimental (DIC)	3.43 mm	3.61 mm	3.61 mm	3.39 mm
Numerical Model prediction	3.60 mm	3.62 mm	3.51 mm	3.23 mm
Error	4.9%	3.9%	2.8%	4.5%
U1 = 0.7 mm	Geometry A	Geometry B	Geometry C	Geometry D
Experimental (DIC)	4.25 mm	4.18 mm	-	-
Numerical Model prediction	4.28 mm	4.32 mm	-	-
Error	0.6%	3.3%		

Table 4. Comparation in direction 3 between experimental and predicted values for different values of U1.

The model predicts the displacement value in direction 3 with an error of 5.3%, which is an acceptable value. Table 4 presents a comparison between experimental values measured with 3D DIC and numerical model prediction of the maximum displacement in direction 3, out of the plane of the laminate. Differences are produced mainly by small misalignments of the specimens

in the experimental setup. This is perceptible because curved contour plots are observed in the DIC images compared to the numerical models, which, being ideal, do not consider these possible misalignments.

Plate without delamination   **Plate with delamination**
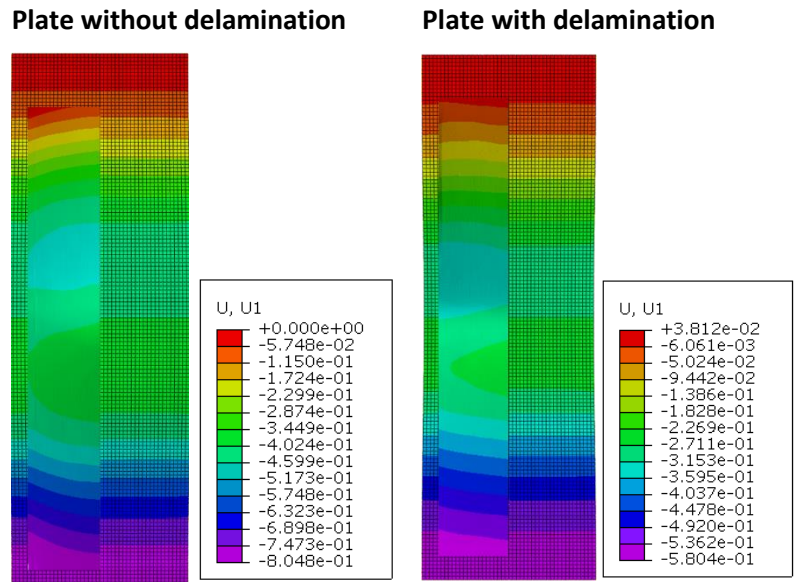
Figure 10: Comparison of the displacements in direction 1 between Abaqus and DIC 3D for geometries A and C.

**Plate without delamination**   **Plate with delamination**
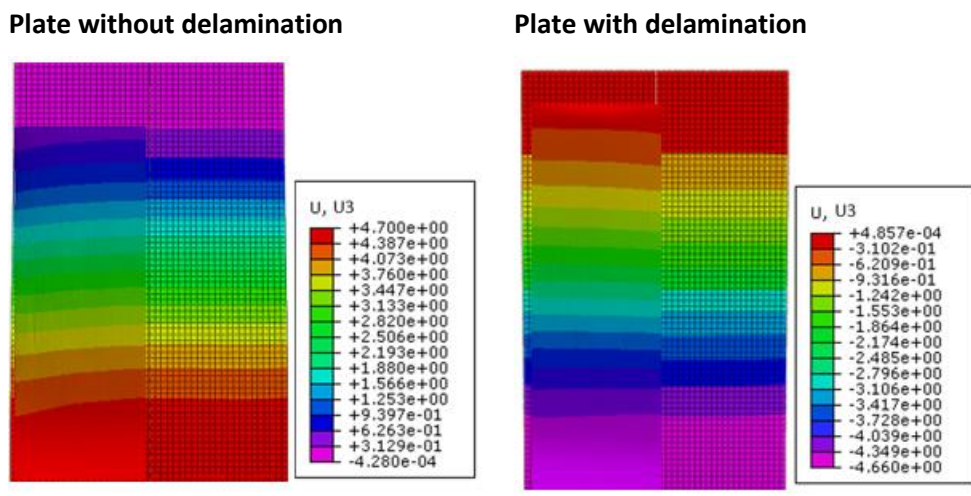
**Figure 11:** Comparison of the displacements in direction 3 between Abaqus and DIC 3D for geometries A and C.

5.1 Specimens without delamination

Once the models have been validated, the numerical results obtained and the type of failure that appears are analyzed for the different geometries. In Fig. 12, the numerical and experimental load are compared, including the mean and the standard deviation of the experimental tests until reaching the first ply failure. The numerical model presents good agreement with the experimental curve, the peak load is also estimated with good precision with an error of 7.0%. Global buckling mode is predicted, corresponding to this type of geometry, as mentioned in the experimental section.

It was also observed that delamination initiated at the free edges of the material, producing the fiber breakage of the material in the center of the laminate. This phenomenon is observed in Fig. 13 where the interlaminar and intralaminar damages are presented and agree well with the experimental results shown in Fig. 7(a).
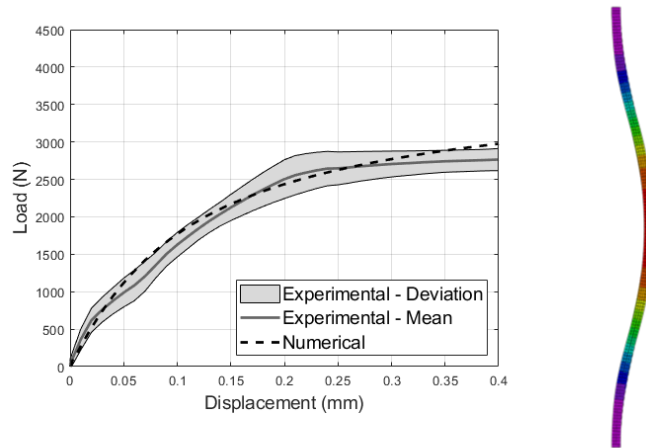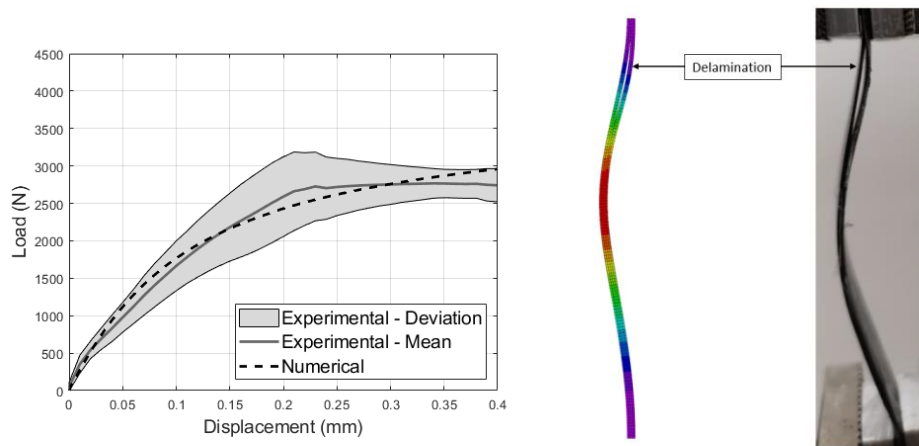

Figure 12: Comparison between experimental and numerical analysis for geometry A.

| (a) | (b) |
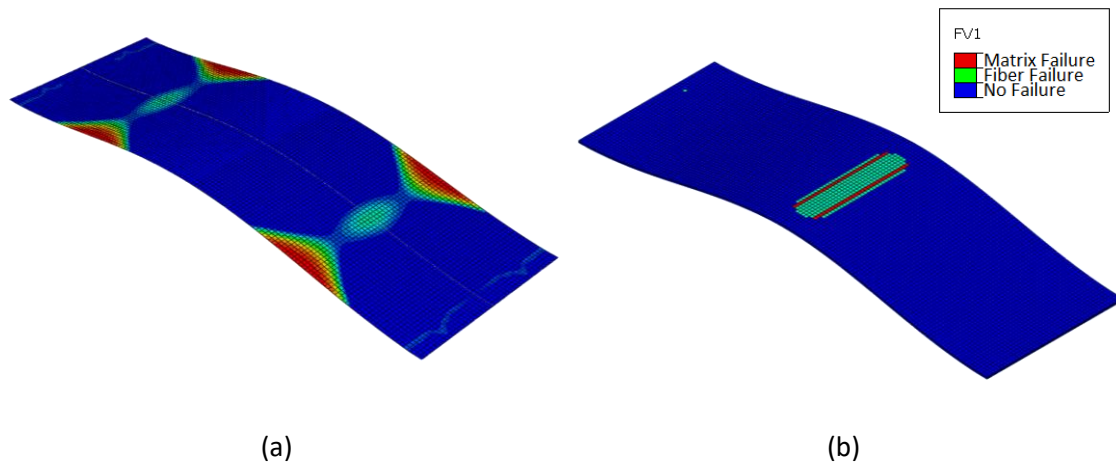
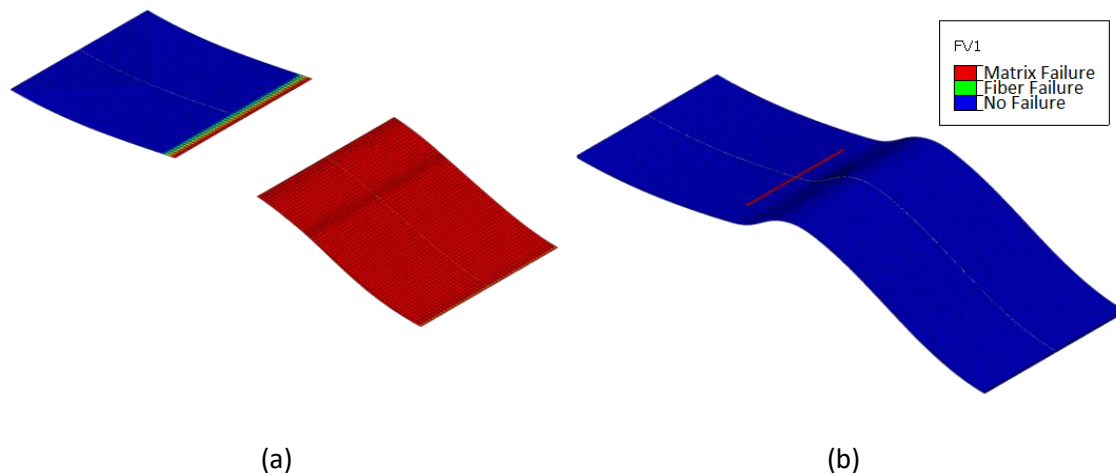**Figure 13:** Delamination damage (a) and intralaminar damage (b) of the geometry A at FPF.

5.2 Specimens with delamination in the middle plane

The configuration B corresponds to a laminate that presents a delamination in the middle plane. In this case, the buckling evolution until first ply failure is similar to that observed in configuration A, as explained in experimental results section. Since the delamination is located in the middle plane, the influence is negligible at the beginning of the test, and the evolution of the curve is almost identical to the case without damage, reaching the same peak load with an error of 6.8% between experimental and numerical model. The model was able to reproduce the initiation of delamination near the grips as shown in Fig. 14.

Figure 14: Comparison between experimental and numerical analysis for geometry B.

The cohesive ply showed that delamination propagated in one direction until reaching the boundary of the laminate, increasing the interlaminar damage. However, it was observed that the peak load is similar to configuration A. This is explained by the fact that the dominant mode is mode II and not mode I, which favors the spread of the delamination. This was observed with the digital image analysis, where the displacement in direction 3 was almost the same for both geometries. On the other hand, matrix damage propagates in perpendicular direction to the delamination direction, reducing the specimen load capacity in a drastic way (see Fig. 15).

(a)   (b)

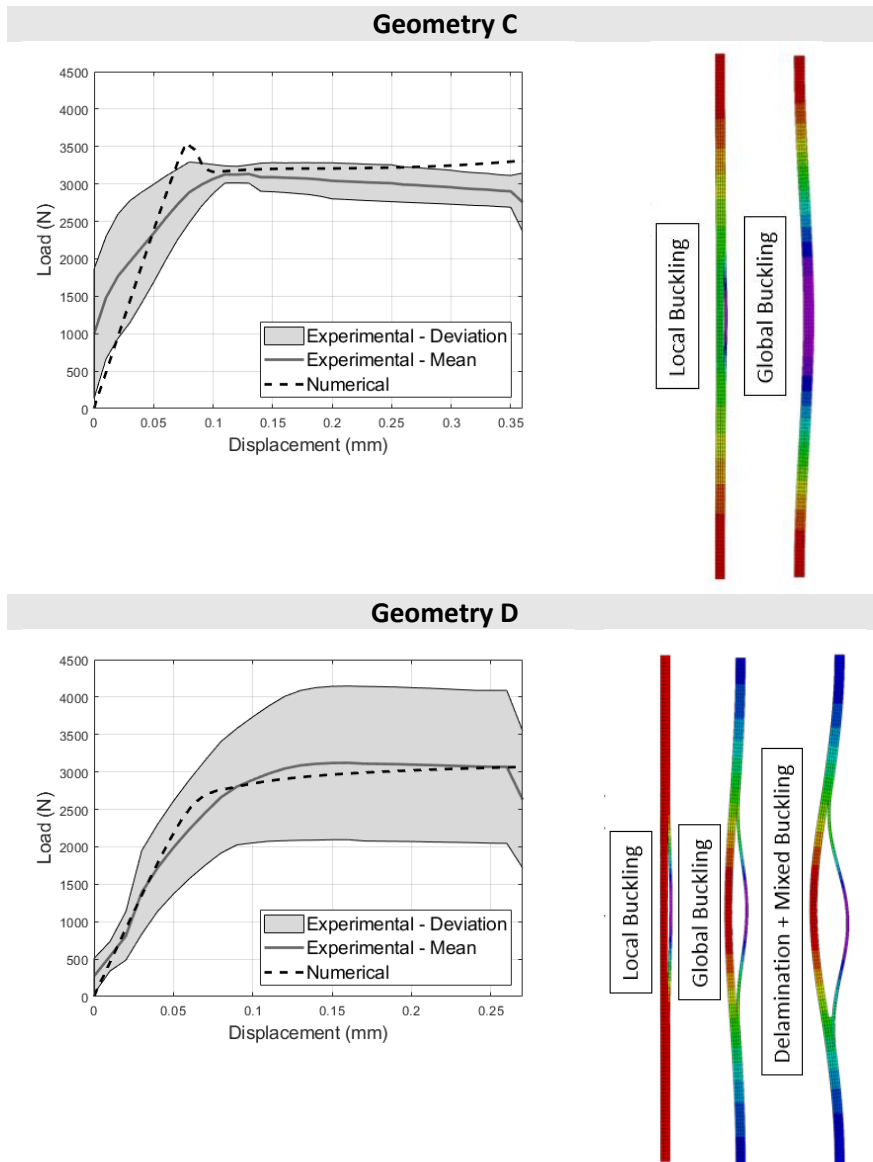**Figure 15:** Delamination damage (a) and intralaminar damage (b) of the geometry B at FPF.

5.3 Specimens with delamination in the upper layer

In the 3rd and 4th batch of specimens, the delamination is located on the external face of the material. This greatly influences the behavior, commented in the experimental analysis.

It is observed that the trends and first ply failure are much more evident in these geometries. The model prediction is quite accurate, and the breaking loads of these plies have been estimated with errors of 11% and 0.5% for the C and D geometries respectively.

In both cases the buckling begins by means of a local buckling, continuing its evolution in a mixed-buckling mode. The external ply that suffers delamination was the first to break due to its curvature involving maximum stresses as seen in Fig. 16. It was also observed that although the maximum load reached for all the geometries is similar, the existence of a delamination near the upper face produces a decrease in the buckling resistance of the material of 38.2% in both

cases with respect to geometry A (free-damage geometry). In the case corresponding with the delamination in the middle plane, this decrease is about of 28.6%.

Figure 16: Comparison between experimental and numerical analysis for geometries C and D.

Analyzing the intralaminar and interlaminar damage, it was observed how the delamination propagates in both directions, increasing the damaged area. Due to the mixed buckling mode, the crack opening mode is Mode I, which is the most unfavorable and therefore the most unstable for thin-walled structures. For both geometries the intralaminar failure is mainly matrix failure, as seen in Fig. 17.
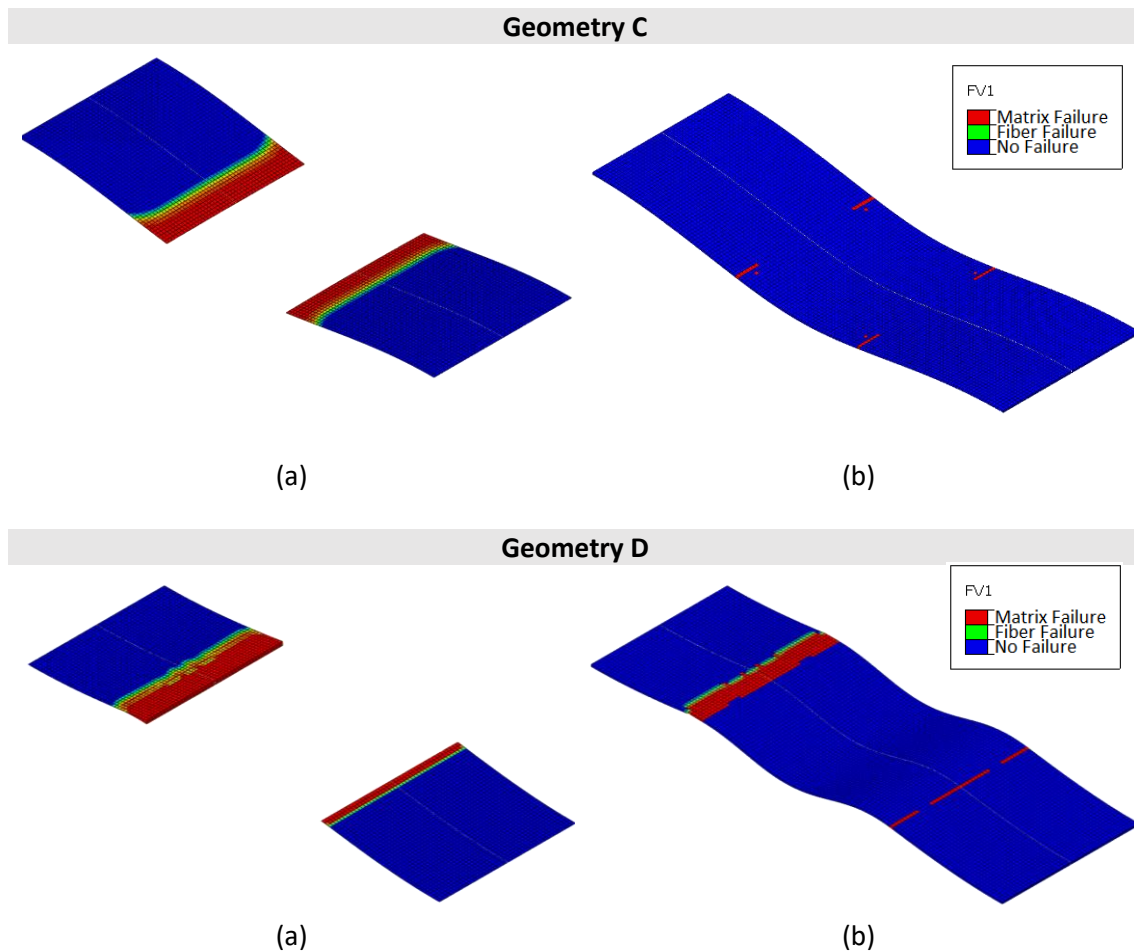
Figure 17: Delamination damage (a) and intralaminar damage (b) of geometries C and D at FPF.

6. Conclusions

This paper presents a numerical and experimental analysis of the influence of delamination on CFRP laminates under compressive load. Four batches of specimens have been manufactured, one without defects and the other three with initial delamination with different length and location. For each of these batches, a numerical model has been developed including a subroutine based on the Hashin criterion to simulate intralaminar damage as well as cohesive elements to simulate interlaminar damage. For the validation of the models, the 3D DIC technique has been applied during experimental tests and the displacement fieldshave been compared, obtaining an average error less than 5.3%.

It has been observed that for the cases where the initial delamination was not at the central plies, a local buckling mode appeared. This causes a stiffer response of the laminate initially, but also causes the failure to appear earlier than in the other cases. Furthermore, a clear relationship between interlaminar and intralaminar failure has been shown. In all cases, interlaminar delamination damage has appeared, followed by a failure of the matrix of the adjacent plies. This matrix damage is followed by a rapid fiber failure leading to overall specimen failure.

Funding

References

[1]   Hocheng H, Tsao CC. The path towards delamination-free drilling of composite materials. J Mater Process Technol 2005;167:251–64. https://doi.org/10.1016/J.JMATPROTEC.2005.06.039.

[2]   Kulkarni P, Mali KD, Singh S. An overview of the formation of fibre waviness and its effect on the mechanical performance of fibre reinforced polymer composites. Compos Part A Appl Sci Manuf 2020;137:106013. https://doi.org/https://doi.org/10.1016/j.compositesa.2020.106013.

[3]   Feito N, Calvo JV, Belda R, Giner E. An experimental and numerical investigation to characterize an aerospace composite material with open-hole using non-destructive techniques. Sensors (Switzerland) 2020;20:1–18. https://doi.org/10.3390/s20154148.

[4]   Feito N, Díaz-Álvarez J, Díaz-Álvarez A, Cantero JL, López-Puente J, Miguelez H. Influence of tool geometry in drilling CFRP. 16th Eur. Conf. Compos. Mater. ECCM 2014, 2014.

[5]   Shen L, Liu L, Zhou Y, Wu Z. Thickness effect of carbon nanotube interleaves on free-edge delamination and ultimate strength within a symmetric composite laminate. Compos Part A Appl Sci Manuf 2020;132:105828. https://doi.org/10.1016/j.compositesa.2020.105828.

[6]   Woigk W, Hallett SR, Jones MI, Kuhtz M, Hornig A, Gude M. Experimental investigation of the effect of defects in Automated Fibre Placement produced composite laminates. Compos Struct 2018;201:1004–17. https://doi.org/10.1016/j.compstruct.2018.06.078.

[7]   Ouyang T, Sun W, Guan Z, Tan R, Li Z. Experimental study on delamination growth of stiffened composite panels in compression after impact. Compos Struct 2018;206:791–800. https://doi.org/10.1016/j.compstruct.2018.08.080.

[8]   Sun XC, Hallett SR. Failure mechanisms and damage evolution of laminated composites under compression after impact (CAI): Experimental and numerical study. Compos Part A Appl Sci Manuf 2018;104:41–59. https://doi.org/https://doi.org/10.1016/j.compositesa.2017.10.026.

[9]   Shah SZH, Megat-Yusoff PSM, Karuppanan S, Choudhry RS, Ud Din I, Othman AR, et al. Compression and buckling after impact response of resin-infused thermoplastic and thermoset 3D woven composites. Compos Part B Eng 2021;207:108592. https://doi.org/10.1016/J.COMPOSITESB.2020.108592.

[10]   Zou J, Lei Z, Bai R, Liu D, Jiang H, Liu J, et al. Damage and failure analysis of composite stiffened panels under low-velocity impact and compression after impact. Compos Struct 2021;262:113333. https://doi.org/10.1016/J.COMPSTRUCT.2020.113333.

[11]   Lapczyk I, Hurtado JA. Progressive damage modeling in fiber-reinforced materials. Compos Part A Appl Sci Manuf 2007;38:2333–41. https://doi.org/10.1016/J.COMPOSITESA.2007.01.017.

[12]   Rozylo P. Experimental-numerical study into the stability and failure of compressed thin-walled composite profiles using progressive failure analysis and cohesive zone model. Compos Struct 2021;257:113303.

https://doi.org/10.1016/J.COMPSTRUCT.2020.113303.

[13]   Gamstedt EK, Talreja R. Fatigue damage mechanisms in unidirectional carbon-fibre-reinforced plastics. J Mater Sci 1999;34:2535–46. https://doi.org/10.1023/A:1004684228765.

[14]   Rzeczkowski J, Samborski S, Moura M de. Experimental investigation of delamination in composite continuous fiber-reinforced plastic laminates with elastic couplings. Materials (Basel) 2020;13:1–17. https://doi.org/10.3390/ma13225146.

[15]   Sajjadi SH, Salimi-Majd D, Ostad Ahmad Ghorabi MJ. Development of a brittle fracture criterion for prediction of crack propagation path under general mixed mode loading. Eng Fract Mech 2016;155:36–48. https://doi.org/10.1016/J.ENGFRACMECH.2016.01.015.

[16]   Shabanijafroudi N, Ganesan R. A new methodology for buckling, postbuckling and delamination growth behavior of composite laminates with delamination. Compos Struct 2021;268:113951. https://doi.org/10.1016/j.compstruct.2021.113951.

[17]   Reddy JN, Pandey AK. A first-ply failure analysis of composite laminates. Comput Struct 1987;25:371–93. https://doi.org/10.1016/0045-7949(87)90130-1.

[18]   Nixon-Pearson OJ, Hallett SR, Withers PJ, Rouse J. Damage development in open-hole composite specimens in fatigue. Part 1: Experimental investigation. Compos Struct 2013;106:882–9. https://doi.org/10.1016/J.COMPSTRUCT.2013.05.033.

[19]   Senck S, Scheerer M, Revol V, Plank B, Hannesschläger C, Gusenbauer C, et al. Microcrack characterization in loaded CFRP laminates using quantitative two- and three-dimensional X-ray dark-field imaging. Compos Part A Appl Sci Manuf 2018;115:206–14. https://doi.org/https://doi.org/10.1016/j.compositesa.2018.09.023.

[20]   Zhang H, Li C, Dai W, Liu Y, Tian S, Huang W, et al. Static compression testing CFRP single-lap composited joints using X-ray µCT. Compos Struct 2020;234:111667. https://doi.org/10.1016/J.COMPSTRUCT.2019.111667.

[21]   Garcea SC, Wang Y, Withers PJ. X-ray computed tomography of polymer composites. Compos Sci Technol 2018;156:305–19. https://doi.org/https://doi.org/10.1016/j.compscitech.2017.10.023.

[22]   Espadas-Escalante JJ, Isaksson P. A study of induced delamination and failure in woven composite laminates subject to short-beam shear testing. Eng Fract Mech 2019;205:359–69. https://doi.org/10.1016/J.ENGFRACMECH.2018.10.015.

[23]   Arumugam V, Saravanakumar K, Santulli C. Damage characterization of stiffened glass-epoxy laminates under tensile loading with acoustic emission monitoring. Compos Part B Eng 2018;147:22–32. https://doi.org/https://doi.org/10.1016/j.compositesb.2018.04.031.

[24]   Tabrizi IE, Khan RMA, Massarwa E, Zanjani JSM, Ali HQ, Demir E, et al. Determining tab material for tensile test of CFRP laminates with combined usage of digital image correlation and acoustic emission techniques. Compos Part A Appl Sci Manuf 2019;127:105623. https://doi.org/10.1016/J.COMPOSITESA.2019.105623.

[25]   Feng W, Zhou X, Zeng X, Yang C. Ultrasonic inspection of localized defects in low-porosity CFRP. Sensors (Switzerland) 2019;19. https://doi.org/10.3390/s19071654.

[26]   Dattoma V, Willem Panella F, Pirinu A, Saponaro A. Ultrasonic and thermographic

studies for CFRP inspections with real and simulated defects. Mater Today Proc 2020. https://doi.org/https://doi.org/10.1016/j.matpr.2020.02.915.

[27]   Panella FW, Pirinu A. Thermal and ultrasonic analysis of fatigue damaged CFRP samples under traction and bending load. Procedia Struct Integr 2020;28:1709–18. https://doi.org/10.1016/j.prostr.2020.10.146.

[28]   Hashin Z. Failure Criteria for Unidirectional Fiber Composites. J Appl Mech 1980;47:329–34. https://doi.org/10.1115/1.3153664.

[29]   Wysmulski P, Debski H, Falkowicz K. Stability analysis of laminate profiles under eccentric load. Compos Struct 2020;238:111944. https://doi.org/10.1016/j.compstruct.2020.111944.

[30]   Lasri L, Nouari M, El Mansori M. Modelling of chip separation in machining unidirectional FRP composites by stiffness degradation concept. Compos Sci Technol 2009;69:684–92. https://doi.org/10.1016/J.COMPSCITECH.2009.01.004.

[31]   Wang D, He X, Xu Z, Jiao W, Yang F, Jiang L, et al. Study on Damage Evaluation and Machinability of UD-CFRP for the Orthogonal Cutting Operation Using Scanning Acoustic Microscopy and the Finite Element Method. Materials (Basel) 2017;10:204. https://doi.org/10.3390/ma10020204.

[32]   Ameri B, Moradi M, Mohammadi B, Salimi-Majd D. Investigation of nonlinear post-buckling delamination in curved laminated composite panels via cohesive zone model. Thin-Walled Struct 2020;154:106797. https://doi.org/10.1016/j.tws.2020.106797.

[33]   Falkowicz K, Ferdynus M, Rozylo P. Experimental and numerical analysis of stability and failure of compressed composite plates. Compos Struct 2021;263:113657. https://doi.org/10.1016/j.compstruct.2021.113657.

[34]   Wang P, Huang X, Wang Z, Geng X, Wang Y. Buckling and Post-Buckling Behaviors of a Variable Stiffness Composite Laminated Wing Box Structure. Appl Compos Mater 2018;25:449–67. https://doi.org/10.1007/s10443-017-9643-3.

[35]   Liu PF, Gu ZP, Peng XQ, Zheng JY. Finite element analysis of the influence of cohesive law parameters on the multiple delamination behaviors of composites under compression. Compos Struct 2015;131:975–86. https://doi.org/10.1016/j.compstruct.2015.06.058.

[36]   Hwang SF, Liu GH. Buckling behavior of composite laminates with multiple delaminations under uniaxial compression. Compos Struct 2001;53:235–43. https://doi.org/10.1016/S0263-8223(01)00007-1.

[37]   Liu PF, Zheng JY. On the through-the-width multiple delamination, and buckling and postbuckling behaviors of symmetric and unsymmetric composite laminates. Appl Compos Mater 2013;20:1147–60. https://doi.org/10.1007/s10443-013-9321-z.

[38]   Aydin Komur M, Sen F, Ataş A, Arslan N. Buckling analysis of laminated composite plates with an elliptical/circular cutout using FEM. Adv Eng Softw 2010;41:161–4. https://doi.org/10.1016/J.ADVENGSOFT.2009.09.005.

[39]   Chai H, Babcock CD, Knauss WG. One dimensional modelling of failure in laminated plates by delamination buckling. Int J Solids Struct 1981;17:1069–83. https://doi.org/10.1016/0020-7683(81)90014-7.

[40]   Bruno D, Greco F. An asymptotic analysis of delamination buckling and growth in

layered plates. Int J Solids Struct 2000;37:6239–76. https://doi.org/10.1016/S0020-7683(99)00281-4.

[41]   Köllner A, Kashtalyan M, Guz I, Völlmecke C. On the interaction of delamination buckling and damage growth in cross-ply laminates. Int J Solids Struct 2020;202:912–28. https://doi.org/10.1016/J.IJSOLSTR.2020.05.035.

[42]   Zhuo XR, Jang HS, Beom HG. Delamination buckling of a thin film bonded to an orthotropic substrate. Int J Precis Eng Manuf 2015;16:323–33. https://doi.org/10.1007/s12541-015-0043-z.

[43]   Xue J, Jin F, Zhang J, Li P, Xia F, Xu J, et al. Post-buckling induced delamination propagation of composite laminates with bi-nonlinear properties and anti-penetrating interaction effects. Compos Part B Eng 2019;166:148–61. https://doi.org/10.1016/J.COMPOSITESB.2018.11.082.

[44]   Barbero EJ, Reddy JN. Modeling of delamination in composite laminates using a layer-wise plate theory. Int J Solids Struct 1991;28:373–88. https://doi.org/10.1016/0020-7683(91)90200-Y.

[45]   Wang K, Zhao L, Hong H, Gong Y, Zhang J, Hu N. An analytical model for evaluating the buckling, delamination propagation, and failure behaviors of delaminated composites under uniaxial compression. Compos Struct 2019;223:110937. https://doi.org/10.1016/J.COMPSTRUCT.2019.110937.

[46]   Wang K, Zhao L, Hong H, Zhang J, Hu N. An extended analytical model for predicting the compressive failure behaviors of composite laminate with an arbitrary elliptical delamination. Int J Solids Struct 2020;185–186:439–47. https://doi.org/10.1016/J.IJSOLSTR.2019.09.002.

[47]   Krueger R. Virtual crack closure technique: History, approach, and applications . Appl Mech Rev 2004;57:109–43. https://doi.org/10.1115/1.1595677.

[48]   Shivakumar KN, Tan PW, Newman JC. A virtual crack-closure technique for calculating stress intensity factors for cracked three dimensional bodies. Int J Fract 1988;36:R43–50. https://doi.org/10.1007/BF00035103.

[49]   Park K, Paulino GH. Cohesive Zone Models: A Critical Review of Traction-Separation Relationships Across Fracture Surfaces. Appl Mech Rev 2013;64. https://doi.org/10.1115/1.4023110.

[50]   de Borst R. Numerical aspects of cohesive-zone models. Eng Fract Mech 2003;70:1743–57. https://doi.org/10.1016/S0013-7944(03)00122-X.

[51]   Buchholz FG, Grebner H, Dreyer KH, Krome H. 2D- and 3D-Applications of the Improved and Generalized Modified Crack Closure Integral Method. Comput Mech '88 1988:387–90. https://doi.org/10.1007/978-3-642-61381-4_94.

[52]   Suemasu H, Kumagai T. Compressive Behavior of Multiply Delaminated Composite Laminates Part 2: Finite Element Analysis. AIAA J 1998;36:1286–90. https://doi.org/10.2514/2.512.

[53]   Riccio A, Perugini P, Scaramuzzino F. Modelling compression behaviour of delaminated composite panels. Comput Struct 2000;78:73–81. https://doi.org/10.1016/S0045-7949(00)00106-1.

[54]   Raimondo A, Doesburg SA, Bisagni C. Numerical study of quasi-static and fatigue

delamination growth in a post-buckled composite stiffened panel. Compos Part B Eng 2020;182:107589. https://doi.org/10.1016/J.COMPOSITESB.2019.107589.

[55] Feito N, Álvarez JD, Cantero JL, Miguélez MH. Influence of Special Tool Geometry in Drilling Woven CFRPs Materials. Procedia Eng., vol. 132, 2015, p. 632–8. https://doi.org/10.1016/j.proeng.2015.12.541.

[56] De Cicco D, Taheri F. Delamination Buckling and Crack Propagation Simulations in Fiber-Metal Laminates Using xFEM and Cohesive Elements. Appl Sci 2018;8. https://doi.org/10.3390/app8122440.

[57] Mekonnen AA, Woo K, Kang M, Kim IG. Effects of Size and Location of Initial Delamination on Post-buckling and Delamination Propagation Behavior of Laminated Composites. Int J Aeronaut Sp Sci 2020;21:80–94. https://doi.org/10.1007/s42405-019-00195-0.

[58] Turon A, Dávila CG, Camanho PP, Costa J. An engineering solution for mesh size effects in the simulation of delamination using cohesive zone models. Eng Fract Mech 2007;74:1665–82. https://doi.org/10.1016/j.engfracmech.2006.08.025.

[59] Dávila CG, Camanho PP, de Moura MF. Mixed-mode decohesion elements for analyses of progressive delamination. 19th AIAA Appl Aerodyn Conf 2001. https://doi.org/10.2514/6.2001-1486.

[60] Wang RG, Zhang L, Zhang J, Liu WB, He XD. Numerical analysis of delamination buckling and growth in slender laminated composite using cohesive element method. Comput Mater Sci 2010;50:20–31. https://doi.org/10.1016/J.COMMATSCI.2010.07.003.

[61] Hosseini Toudeshky H, Hosseini S, Mohammadi B. Delamination buckling growth in laminated composites using layerwise-interface element. Compos Struct 2010;92:1846–56. https://doi.org/10.1016/J.COMPSTRUCT.2010.01.013.

[62] ASTM International. Standard Test Method for Compressive Properties of Polymer Matrix Composite Materials. ASTM Int 2016;03:1–13. https://doi.org/10.1520/D3410.

[63] Lee J, Gurdal Z, Griffin OH. Postbuckling of laminated composites with delaminations. AIAA J 1995;33:1963–70. https://doi.org/10.2514/3.12752.